Device

Article

An inkjet-printable organic electrochemical transistor array with differentiated ion dynamics for sweat fingerprint identification

Graphical abstract

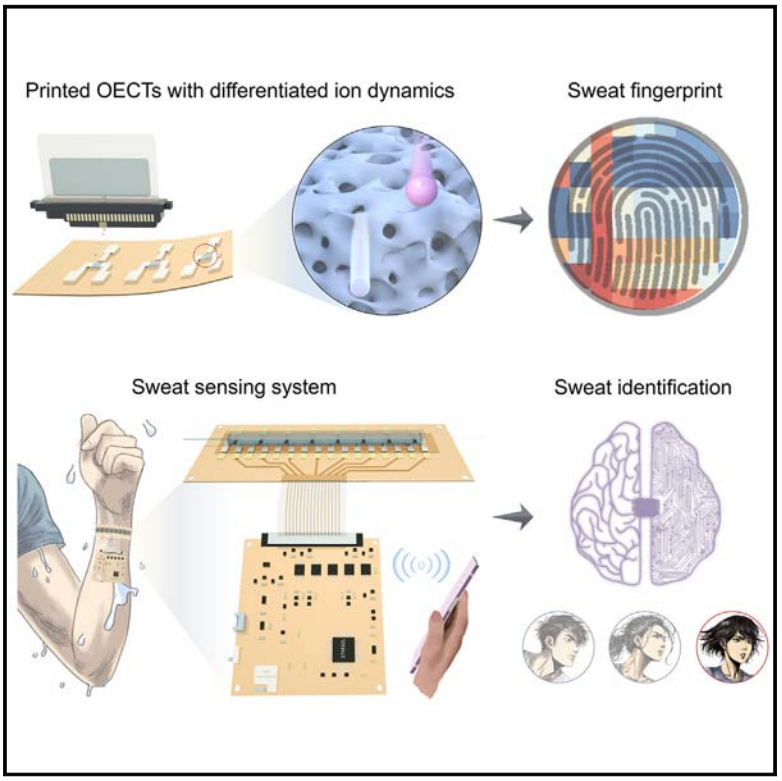

Highlights

- An ion dynamics-dependent sweat fingerprint identification strategy
- An OECT array with differentiated and customized ion dynamics was inkjet printed
- A flexible wireless peripheral system was developed for sweat identification
- An AI model for identifying sweat from different users was demonstrated

Authors

Dongzi Yang, Junchang Wang, Miaoyi Xu, ..., Lizhen Huang, Ming Wang, Yuanlong Shao

Correspondence

lzhuang@suda.edu.cn (L.H.), wang_ming@fudan.edu.cn (M.W.), shaoyuanlong@pku.edu.cn (Y.S.)

In brief

Yang et al. present an ion dynamics-dependent strategy for sweat identification, utilizing an inkjet-printed organic electrochemical transistor (OECT) array. The OECT array generates differentiated dynamic electrochemical responses for specific sweat components, enabling the construction of ion dynamics-based fingerprints. Through system-level integration and AI algorithm assistance, the device enables wireless sweat monitoring and biochemical fingerprint identification for personal health monitoring.

Yang et al., 2025, Device *3*, 100651
April 18, 2025
https://doi.org/10.1016/j.device.2024.100651

Please cite this article in press as: Yang et al., An inkjet-printable organic electrochemical transistor array with differentiated ion dynamics for sweat fingerprint identification, Device (2024), https://doi.org/10.1016/j.device.2024.100651

Device

CellPress
OPEN ACCESS

Article

An inkjet-printable organic electrochemical transistor array with differentiated ion dynamics for sweat fingerprint identification

Dongzi Yang,[1,2,3,8] Junchang Wang,[2,3,8] Miaoyi Xu,[1] Xiaoling Tong,[1] Yishan Cao,[3] Jie Lu,[4] Jie Qiu,[2] Pei Chen,[2] Jinrong Luo,[3] Liang Zhang,[3] Cheng Shi,[4] Yanyan Shao,[1,3] Zhou Xia,[3] Qian Xu,[2] Jie Cao,[2] Zhi Zhang,[1,7] Ting Lei,[1,7] Lizhen Huang,[4,*] Ming Wang,[2,*] and Yuanlong Shao[1,5,6,9,*]

[1]School of Materials Science and Engineering, Peking University, Beijing 100871, P.R. China
[2]State Key Laboratory of Integrated Chips and Systems, Frontier Institute of Chip and System, Fudan University, Shanghai 200433, P.R. China
[3]College of Energy, Soochow Institute for Energy and Materials Innovations (SIEMIS), Key Laboratory for Advanced Carbon Materials and Wearable Energy Technologies of Jiangsu Province, SUDA-BGI Collaborative Innovation Center, Soochow University, Suzhou 215006, P.R. China
[4]Institute of Functional Nano & Soft Materials (FUNSOM), Jiangsu Key Laboratory for Carbon-based Functional Materials & Devices, Soochow University, Suzhou 215123, P.R. China
[5]Academy for Advanced Interdisciplinary Studies, Peking University, Beijing 100871, P.R. China
[6]Beijing Graphene Institute (BGI), Beijing 100095, China
[7]Key Laboratory of Polymer Chemistry and Physics of Ministry of Education, Peking University, Beijing 100871, P.R. China
[8]These authors contributed equally
[9]Lead contact
*Correspondence: lzhuang@suda.edu.cn (L.H.), wang_ming@fudan.edu.cn (M.W.), shaoyuanlong@pku.edu.cn (Y.S.)
https://doi.org/10.1016/j.device.2024.100651

THE BIGGER PICTURE Sweat offers a wealth of insights into our body's condition, from hydration balance to markers of certain diseases. However, effectively monitoring sweat is challenging due to its complex mix of ions and molecules. Current sweat monitoring devices tend to rely on selective sensors with specific bio-recognition elements (e.g., ion-selective membranes [ISMs] and enzymes) to selectively bind with certain ions or molecules. However, the complex chemical modifications in these sensors, along with susceptibility to interference and signal drift, limits their broader application. This work leverages intrinsic ion dynamics within an organic electrochemical transistor (OECT) array to detect and analyze sweat content. Assisted by an AI algorithm, this device can interpret ion patterns in collected sweat to give health insights. This advancement in sweat sensing facilitates non-invasive wearable health monitors, providing an effective tool for personal wellness and clinical diagnostics.

SUMMARY

Sweat contains physiological information for non-invasive health monitoring. However, the complexity of sweat components makes signal decoupling challenging; this traditionally relies on selective sensors to detect specific biomarkers and manual analysis for decoupling, which are susceptible to interference and signal drift. In this study, we present an intrinsic ion dynamics-dependent sweat identification strategy by combining an inkjet-printed customized organic electrochemical transistor (OECT) array with artificial intelligence (AI) algorithms. The OECT array comprises two types of channel films, featuring 3D-interconnected porous (3D-IP) structures with facilitated ion transport and tabular porous (TP) structures with enhanced electron transport. The designed OECT array achieves a differentiated dynamic electrochemical response for specific sweat components, thereby constructing ion dynamics-based fingerprint information for sweat identification. Integrated with flexible peripheral circuitry and a convolutional neural network, the OECT array can distinguish six samples of artificial sweat and four samples of real sweat with accuracies of 95.0% and 98.0%, respectively.

INTRODUCTION

Sweat, with its abundant physiological information, is a valuable and non-invasive modality for health monitoring.[1] Ions, serving as omnipresent physiological regulators, play integral roles in modulating blood pH, pressure, and cell membrane permeability.[2] The ion composition in sweat provides insights into a broad spectrum of internal bodily information.[3] Recent advancements in the

Please cite this article in press as: Yang et al., An inkjet-printable organic electrochemical transistor array with differentiated ion dynamics for sweat fingerprint identification, Device (2024), https://doi.org/10.1016/j.device.2024.100651

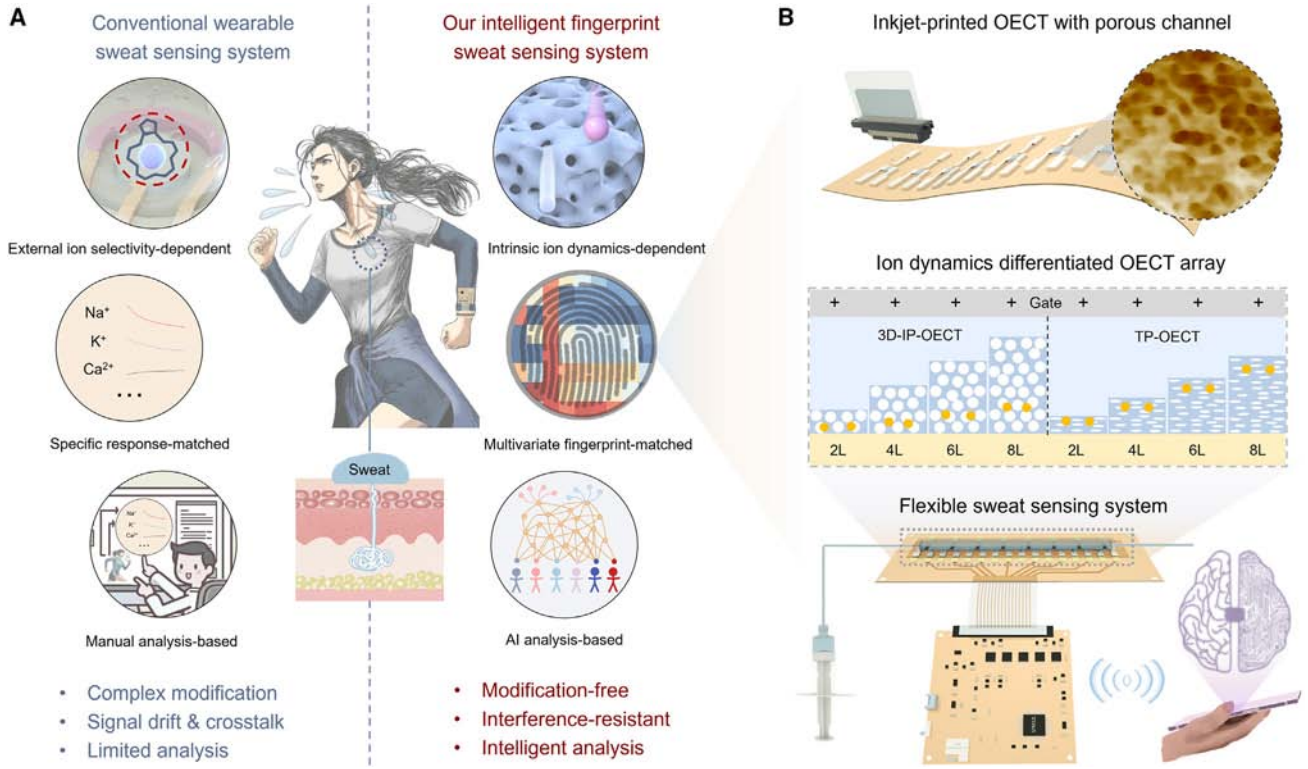

Figure 1. Design of the ion dynamics-differentiated intelligent sweat fingerprint-sensing system

(A) Comparison between a conventional wearable sweat-sensing system (left) and our intelligent sweat fingerprint sensing system (right).

(B) Schematic of our inkjet-printed ion dynamics-differentiated OECT array and a multichannel sweat sensing system.

modification of biorecognition elements (e.g., enzymes, antibodies, ion-selective membranes [ISMs], etc.) that can enable a sensor to selectively detect the specific biomarker in sweat have accelerated the development of sweat sensing and identification systems.[4–6] To obtain ion information from sweat, ISMs can be modified on electrodes to create potential interface changes by selectively binding ions from sweat, allowing sensors to specifically detect certain ions and gather comprehensive ion information through different modifications.[7–10] However, such modifications necessitate complex chemical designs and additional coating processes, and the introduced interfaces resulting from these modifications can lead to instability of the sensor signals.[11] Furthermore, the reliance on absolute and relative signal decoupling schemes is often compromised by the crosstalk from complex targets.[12] Additionally, extensive data from multiple sweat sensors mainly depend on manual analysis (i.e., the process of human intervention in calibrating sensor data and associating them with specific conditions), and deciphering the complex and subtle sweat signals remains labor intensive (Figure 1A).[13,14] Therefore, it is imperative to develop a paradigm for sweat sensing and identification with the merits of modification-free, interference-resistant, and intelligent analysis for practical applications.

Organic electrochemical transistors (OECTs) are attractive ion-sensing components due to their intrinsic ionic-electronic coupling characteristics, signal amplification capability, and solution operability.[15,16] In OECTs, under the influence of gate voltage, ions migrate through the conductive polymer channel film, leading to dedoping and current changes.[17] Different microstructural characteristics, such as porosity and crystallinity, significantly influence ion migration, resulting in differential ion dynamics and disparate dynamic sensing responses.[18–22] These dynamic sensing responses provide features containing ion information, making them less susceptible to interference.[23] However, the ion dynamics of OECTs have not yet been leveraged effectively as sensing characteristics, and there remains a lack of effective strategies for constructing channel materials that exhibit specific or multiple ion dynamics.[24] Moreover, the features of ion dynamics are difficult to extract using traditional analysis schemes. Artificial intelligence (AI) algorithms can help extract target features from implicit information and train models for recognition, thereby enabling the decoupling of complex and obscure ion dynamics information.[25–27] Furthermore, for wearable real-time monitoring applications, a comprehensive system-level integration considering device packaging, peripheral circuitry, and user interfaces is still needed.[28]

Here, we present an AI-assisted sweat-sensing device using an inkjet-printed ion dynamics-differentiated OECT array (Figures 1A and 1B). The device utilized the ion-electron coupling dynamics of OECTs to detect ions in sweat and map the dynamic response curve into multivariate sweat fingerprints to be classified using AI. Inkjet-printed OECTs with porous poly(3,4-ethylenedioxythiophene):poly(styrenesulfonate) (PEDOT:PSS) channels (i.e.,

Please cite this article in press as: Yang et al., An inkjet-printable organic electrochemical transistor array with differentiated ion dynamics for sweat fingerprint identification, Device (2024), https://doi.org/10.1016/j.device.2024.100651

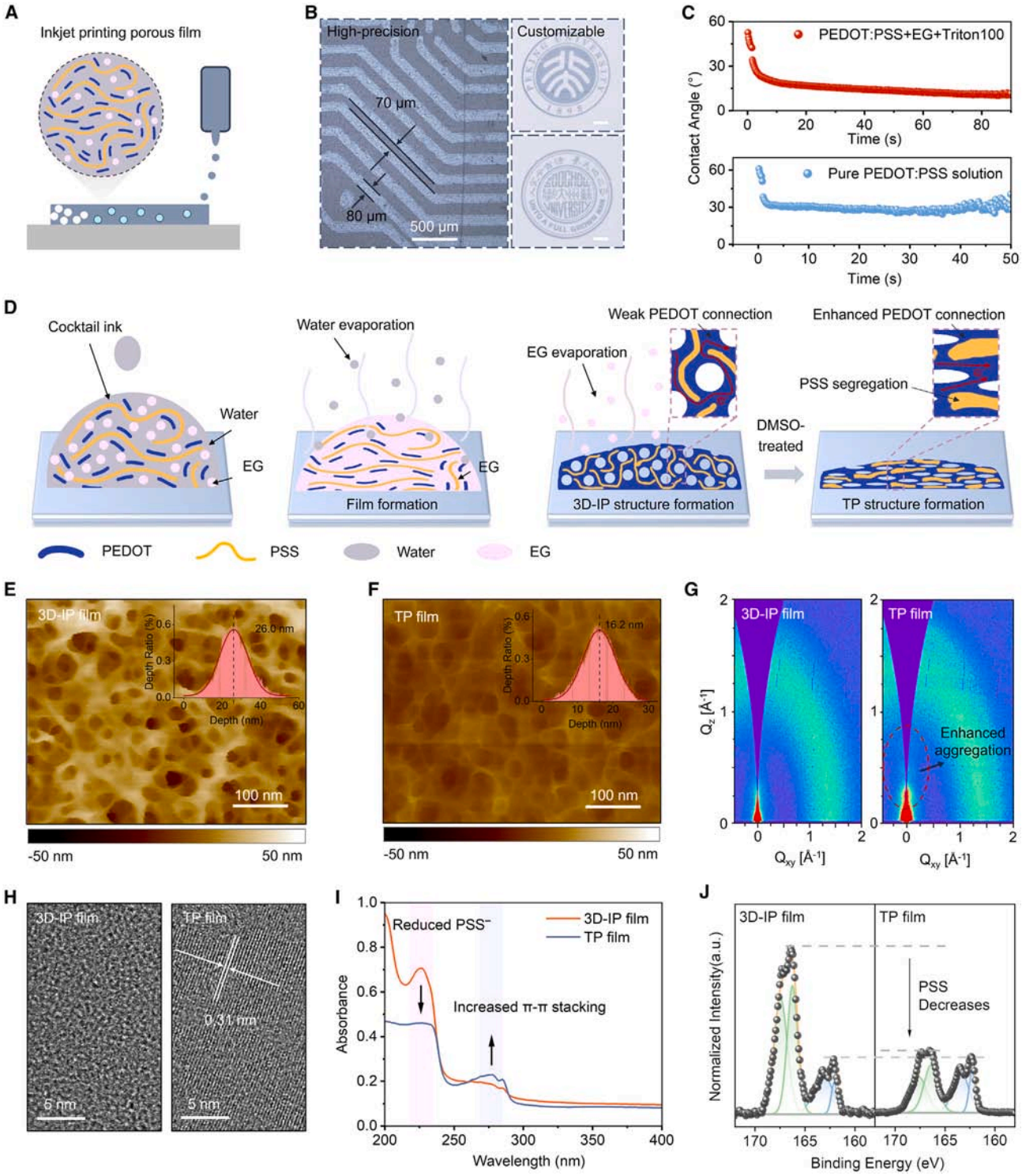

Figure 2. Design of the inkjet-printing process and construction of two types of porous films

(A) Schematic of the inkjet printing process.

(B) Demonstration of high-precision, customizable inkjet-printed PEDOT:PSS patterns. Scale bar of the printed school logos: 2 mm.

(C) Temporal evolution of contact angles of PEDOT cocktail solution and pure PEDOT:PSS solution.

(D) Schematic of the two types of porous film formation processes, including cocktail solution injection, water evaporation, EG evaporation (3D-IP film formation), and DMSO post treatment (TP film formation).

(legend continued on next page)

Please cite this article in press as: Yang et al., An inkjet-printable organic electrochemical transistor array with differentiated ion dynamics for sweat fingerprint identification, Device (2024), https://doi.org/10.1016/j.device.2024.100651

3D-interconnected porous [IP] and tabular porous [TP] films) were investigated. The 3D-IP-OECT presents a facilitating ion intercalation, resulting in faster ion dynamics. The TP-OECT, with its compressed porous channel, displayed slower ion dynamics. These disparities in ionic-electronic transport were exploited to construct the ion dynamics-differentiated OECT array using a customized inkjet-printing process. A multichannel flexible wireless peripheral system was developed to collect real-time sweat fingerprint data based on ion dynamics. To uncover the obscured information from complex sweat fingerprints, a convolutional neural network (CNN) model was established, achieving high accuracy in identifying six samples of artificial sweat with varying ionic composition (95.0%) and four samples of real sweat from different volunteers (98.0%).

RESULTS

Inkjet printing process for constructing the porous films

As illustrated in Figure 2A, the inkjet printer droplets fuse into the porous film with customized patterns via non-contact additive manufacturing. We optimized the printing process and found that a substrate temperature of 60°C and droplet spacing of 20 μm provided the best pattern uniformity and precision (Figure S3; Note S1). Highly customized and high-precision (<70 μm) PEDOT:PSS patterns can be manufactured within minutes (Figure 2B). To manipulate the microstructure of printed PEDOT:PSS films, a composite ink comprising PEDOT:PSS, high-boiling-point ethylene glycol (EG), and octylphenol polyethoxylate (Triton X-100) surfactant were employed. The static and time-dependent contact angles were measured to investigate the ink-wetting behavior and solvent evaporation dynamics (Figures 2C and S4). Compared to the pure PEDOT:PSS aqueous solution (28.6°), the initial contact angle of the cocktail ink (16.8°) decreases and exhibits more stable dynamic contact angle variations during the evaporation process. The well-known "coffee ring effect," usually observed during the solvent volatilization of pure PEDOT:PSS dispersion, was inhibited via the Marangoni effect, triggered by the addition of the high-boiling-point solvent of EG and Triton X-100, which leads to a stable volatilization process for creating a macroscopically uniform film (Figure S5).[29,30]

To understand the mechanism and process of microscale porous film formation, a schematic is shown in Figure 2D. The PEDOT:PSS was initially dispersed in a mixture of water, EG, and Triton X-100. The water evaporated rapidly when the substrate was heated to 60°C, while the EG evaporated more slowly due to its much lower saturated vapor pressure and high boiling point of 197.3°C. This solvent evaporation discrepancy triggered local PEDOT:PSS aggregation and phase separation from water-dispersed components, leaving an IP film; i.e., a 3D-IP film. Afterward, DMSO was used to treat the 3D-IP film, inducing the collapse of its 3D pores to form a tabular architecture by partially dissolving PSS, which acted as the agglomerant for the PEDOT:PSS concrete wall and resulting in formation of the TP film.[31] Atomic force microscopy (AFM) was utilized to characterize the microstructure and pore dimension of the 3D-IP film and TP film, as illustrated in Figures 2E and 2F. The 3D-IP film exhibits a 3D-IP structure in a pore size range of ~10–30 nm with a depth of ~26 nm. In contrast, the TP film showed a compressed TP structure in a pore size range of ~20–30 nm with a pore depth of ~16 nm. This tighter structure enhances the contact between PEDOT regions, providing more conductive pathways for electrons. The crystallinity and orientation of the 3D-IP and TP films were then characterized by grazing incidence wide-angle X-ray scattering (GIWAXS). The GIWAXS pattern in Figure 2G for the 3D-IP film displays a broad diffraction ring centered around 1.3 $Å^{-1}$, indicative of its amorphous nature. In comparison, the TP film exhibits a distinct enhancement in the out-of-plane diffraction peak situated around 0.5 $Å^{-1}$ besides the amorphous diffraction ring. This peak confirms an improved vertical ordering along the (100) crystallographic plane within the film. The high-resolution transmission electron microscopy (HR-TEM) images in Figure 2H also resolve the amorphous feature of 3D-IP films and local crystallization of TP films, with the discernible 0.31 nm lattice spacing of the TP film corresponding to the (020) crystal plane, indicative of π-π stacking along the in-plane direction.[32]

The UV-visible (UV-vis) spectra reveal the molecular aggregate structure, as shown in Figure 2I. It depicts a reduction in the absorption peak at 227 nm, indicative of diminished PSS-related absorption in the transition from a 3D-IP to a TP film. The amplification of the peak at 278 nm in the TP film spectrum corresponds to an increase in π-π stacking interactions among PEDOT chains.[33] In addition, the variation in S 2p in X-ray photoelectron spectroscopy also supports the reduction of PSS in TP film (Figure 2J). These spectral changes agree with the observed morphological and X-ray diffraction analyses, which could be attributed to the DMSO-triggered PSS segregation, thus facilitating the contraction of the 3D porous structure.[32] In contrast, spin-coated PEDOT:PSS films made from the same cocktail solution exhibited a dense and amorphous structure, as shown in Figures S7 and S8. This further validates the uniqueness of the inkjet printing approach to fabricate the porous film.

Device design and electrical characterization of inkjet-printed OECTs

The OECTs are constructed based on the porous PEDOT:PSS films as channel and inkjet-printed Ag electrodes as gate, source, and drain electrodes, as shown in Figures 3A and 3B. The Ag surface of the gate electrode was chlorinated to form an Ag/AgCl nonpolarizable electrode to reduce the voltage drop at the gate. Furthermore, a polyvinyl butyral (PVB) protective layer was

(E) AFM image of the 3D-IP film. Inset: the depth histogram follows a Gaussian distribution with a center of 26.0 nm.
(F) AFM image of the TP film. Inset: the depth histogram follows a Gaussian distribution with a center of 16.2 nm.
(G) GIWAXS pattern of the 3D-IP film and TP film.
(H) HRTEM image of the 3D-IP film and TP film.
(I) UV-vis spectrum of the 3D-IP film and TP film.
(J) X-ray S 2p photoelectron spectra of the 3D-IP film and TP film.

Please cite this article in press as: Yang et al., An inkjet-printable organic electrochemical transistor array with differentiated ion dynamics for sweat fingerprint identification, Device (2024), https://doi.org/10.1016/j.device.2024.100651

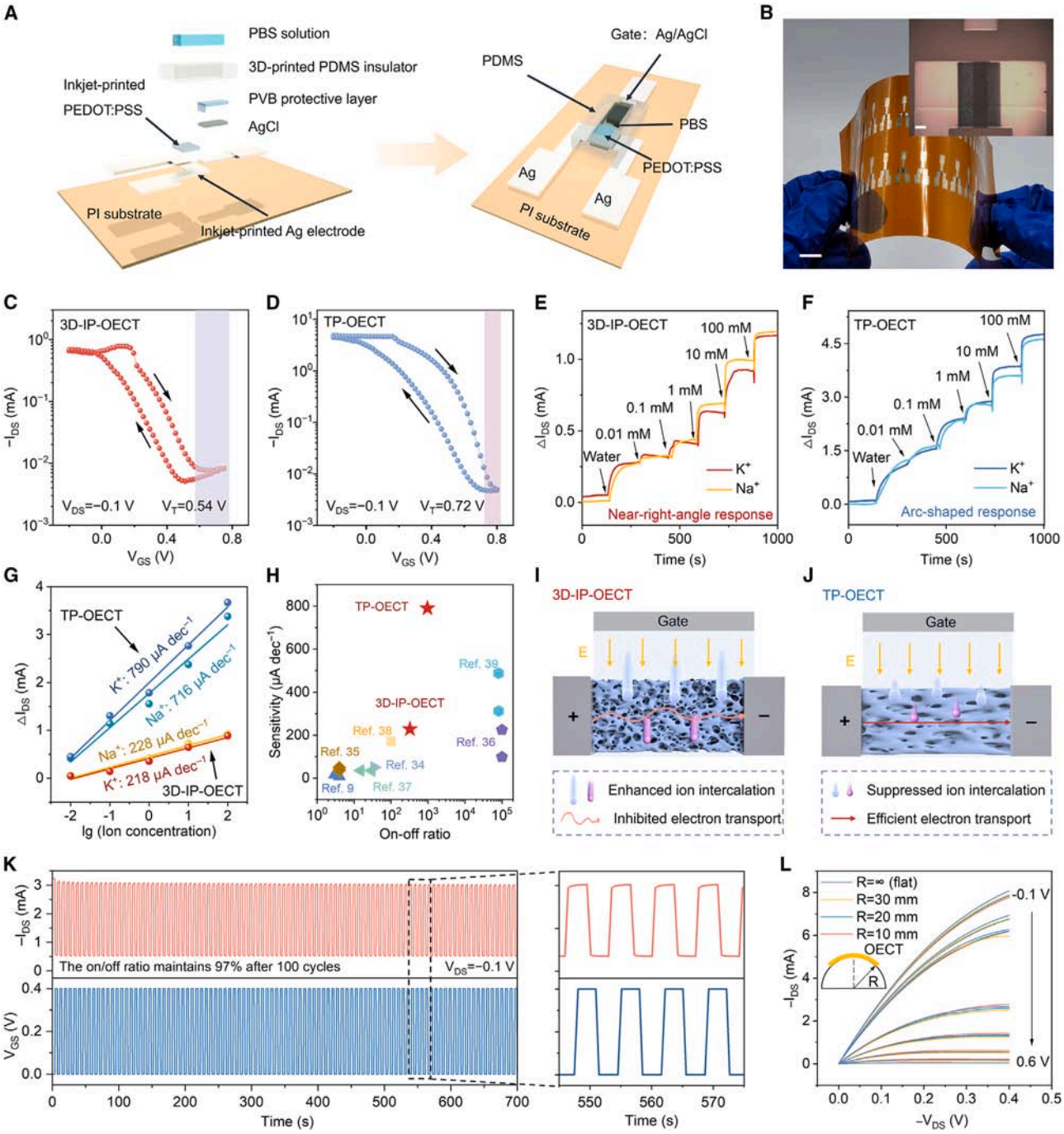

Figure 3. Device design and electrical characterization of fully printed OECTs with two operating modes

(A) The device structure design of the inkjet-printed OECT: anatomy (left) and assembly (right).

(B) Photo of the inkjet-printed OECT array. Scale bar: 1 cm. The inset shows a micrograph of the device. Scale bar: 400 μm.

(C) Transfer characteristic curve of the 3D-IP-OECT.

(D) Transfer characteristic curve of the TP-OECT.

(E) The current response curve of the 3D-IP-OECT under different Na^+ and K^+ concentrations. The curve shows a fast near-right-angle response even when the ion concentration is low.

(F) The current response curve of the TP-OECT under different Na^+ and K^+ concentrations. The curve shows a slow arc-shaped buffer zone response when the ion concentration is low. $V_{DS} = -0.1$, $V_{GS} = 0.4$ V.

(G) The current response value as a function of the logarithmic ion concentration. The slope of the linear fit is used as the sensitivity.

(legend continued on next page)

Please cite this article in press as: Yang et al., An inkjet-printable organic electrochemical transistor array with differentiated ion dynamics for sweat fingerprint identification, Device (2024), https://doi.org/10.1016/j.device.2024.100651

employed to shield the gate electrode from undue oxidation while maintaining a stable potential.[4,14] Before testing, poly(dimethyl) siloxane (PDMS) was 3D printed as an insulation layer and a fixed-size reservoir as a dedicated vessel for the electrolyte.

Figures 3C and 3D displayed the typical depletion-mode transfer characteristic curves of the 3D-IP-OECT and TP-OECT, where the TP-OECT exhibits a higher switching range and a larger voltage window than the 3D-IP-OECT. Notably, the threshold voltages for these two OECTs were calculated as 0.54 V and 0.72 V, respectively (Figure S13). The on-off ratio and transconductance (g_m), which reflect the switching and amplifying capabilities of OECT, are reported in Figure S14. The 3D-IP-OECT achieved an on-off ratio of 325.6 ± 182.8, whereas the TP-OECT demonstrated a higher ratio of 966.1 ± 174.5. The g_m of the 3D-IP-OECT is 5.4 ± 0.5 mS, and that of the TP-OECT could reach 10.8 ± 0.7 mS. The performance comparison with other inkjet-printed OECTs is summarized in Table S1, which highlights the on-off ratio and g_m our device. The single-pulse response characteristics are shown in Figure S16; the 3D-IP-OECT exhibits a faster response speed of 0.40 s than the TP-OECT with 0.74 s, validating the disparity in ion intercalation capability between the two thin films.

The dynamic sensing curve, which captures both current variation and time characteristics to reflect microscopic ion dynamics on a macroscopic scale, was used to evaluate the sensing performance of the 3D-IP-OECT and TP-OECT. The 3D-IP-OECT shows a sharp current response with nearly right-angle shapes under different Na^+ and K^+ concentrations ranging from 0.01 to 100 mM (Figure 3E), which demonstrates the fast ion intercalation in the 3D-IP film. The TP-OECT exhibits a slow current response with arc shapes, especially at low concentrations, which demonstrates the slower ion intercalation in the TP film (Figure 3F). These differences in the dynamic response curve can be used to reflect the intrinsic ion characteristics from different dimensions. Furthermore, the response current was fitted against the logarithm of ion concentration, expressed as the current change per decade (dec) of ion concentration, demonstrating good linearity and sensitivity, as illustrated in Figure 3G. For the 3D-IP-OECT, the sensitivities of K^+ (218 μA dec^{-1}) and Na^+ (228 μA dec^{-1}) were lower compared to the TP-OECT, which exhibited sensitivities of 790 μA dec^{-1} for K^+ and 716 μA dec^{-1} for Na^+. When compared with other OECT-based ion sensors (Figure 3H; Table S2), our device shows higher sensitivity for ion detection, which is important for distinguishing subtle differences in ion concentrations within complex fluids.[9,34–39]

The structure-property interrelationships of the 3D-IP-OECT and TP-OECT are illustrated in Figures 3I and 3J. The porous structure of the 3D-IP film facilitates electrolyte permeation and interaction with the PEDOT:PSS film, resulting in direct dedoping of the inner surface of the pores. The 3D-IP architecture enhances longitudinal ion transport while inhibiting lateral electron transport. As a result, the device exhibits a rapid ion response rate and reaches the off-state limit with a small voltage (~0.6 V). In contrast, the TP film with compressed configuration favors efficient lateral charge transport but suppresses the ion migration from the electrolyte. This necessitates higher energy input for ion intercalation, indicating a higher potential and an elevated driving force, resulting in a slower ion response rate and a larger off-state voltage (~0.8 V). These conclusions are confirmed by the electrochemical impedance data presented in Figure S17. The performance and disparities in their electrical properties highlight the differences in the structure and ion transport dynamics of 3D-IP and TP films, laying a foundation for the development of differentiated sensor arrays.

To evaluate the reliability of OECTs fabricated using inkjet printing technology, we tested their cycling stability and flexibility (Note S3). The cyclic switching stability of OECTs at a sensing gate voltage of 0.4 V is shown in Figure 3K. After 100 pulse cycles, the on-off ratio of the device remained at 97%. The stable performance observed over 1,000 cycles of large-voltage-window (−0.4 V–0.8 V) cyclic voltammetry testing, with 82.6% capacitance retention (Figure S18). Cyclic bending tests with a 2 cm outer bending radius revealed that the resistance changes of the printed OECTs are less than 20% after 10,000 cycles (Figure S19). The output characteristic curves obtained at bending radii of 30, 20, and 10 mm closely overlapped with those under flat conditions, demonstrating negligible impact on device functionality (Figure 3L). The reproducibility of the printed OECT devices is demonstrated by the uniform performance across a large-area array (8 × 4 configuration; Figure S20).

Ion dynamics-differentiated OECT sensing arrays and systems

Based on the designed 3D-IP-OECTs and TP-OECTs, we built a flexible sweat-sensing system for real-time sweat data collection. This system consists of the inkjet-printed OECT array, a microfluidic module, an adapter circuit board, a wireless multichannel test circuit board, and a mobile app (Figure 4A). The system-level block diagram of the system is shown in Figure 4B, including the modules of signal generation, transduction, transmission, and visualization.

To more comprehensively capture the sweat fingerprint information, four 3D-IP-OECTs and four TP-OECTs were configured into 2-, 4-, 6-, and 8-layer printed PEDOT:PSS as channels (Figure 4C).[40] As the thickness of the channel layer increases, the OECT sensing unit takes longer to reach its channel saturation status, resulting in a gradual transition from the right-angle curve to the arc-shaped curve. Combining the channel structure- and thickness-dependent sensing behaviors, the differentiated OECT array reveals the internal information of sweat and forms the ion dynamics-based fingerprint.

Figure 4D illustrates the response curves of the ion dynamics-differentiated OECT array at 1 mM K^+ concentration. The OECT units on the left side of the array show fast response curves close to the right-angle shape due to the larger pore structure

(H) Performance comparison of sensitivity and on-off ratio for OECT-based ion sensors.
(I) Schematic of ion-electron coupling transport of the 3D-IP-OECT.
(J) Schematic of ion-electron coupling transport of the TP-OECT.
(K) Stability of the inkjet-printed OECT tested in an ambient environment. After several voltage-switching cycles, the device can still maintain good performance.
(L) Output characteristic curve of the TP-OECT at bending radii of 30, 20, and 10 mm and flattening.

Please cite this article in press as: Yang et al., An inkjet-printable organic electrochemical transistor array with differentiated ion dynamics for sweat fingerprint identification, Device (2024), https://doi.org/10.1016/j.device.2024.100651

Figure 4. Design of flexible sensing systems and ion dynamics-differentiated OECT arrays

(A) Schematic of the flexible microfluidic-integrated wireless multichannel sensing system.

(B) System-level block diagram showing signal generation, transduction, transmission, and visualization from the microprogrammed control unit to the OECT sensor array and then to the user interface.

(C) Schematic of the inkjet printing customized differentiated array with different ion intercalation dynamics.

(D) Comparison of the response curves of 8 differentiated OECTs at a concentration of 1 mM K^+. On the left, they are close to a near-right-angle response, and on the right, they are close to an arc-shaped response.

(E) Photographs of the flexible system worn on the wrist and a portable mobile app. Scale bar: 4 cm.

(F) Photographs of the entire system worn on the back of the human body demonstrate its system-level conformal characteristics. Scale bars: 8 cm (left) and 2 cm (right).

and thinner channel layer. In contrast, the OECT units on the right side present slow response curves close to the arc shape because of the smaller pore structure and thicker channel layer. The eight units in the array display a consistent linear response to Na^+ and K^+ concentrations ranging from 0.01 to 100 mM (Figures S25–S27), indicating good uniformity. The differential response to Na^+ and K^+ of eight units (Figure S28) demonstrates the potential of the OECT array to identify sweat. Thus, this approach enables an electrical readout ion dynamics-differentiated array, akin to gel electrophoresis utilized in protein analysis, which can be used for sweat component differentiation (Note S4).

In the flexible sweat-sensing system, the sensing curves of eight OECTs could be collected simultaneously through the microfluidic module and the differentiated OECT array, sent to external equipment via wireless transmission, and displayed on the mobile app (Figure S29). The flexible system weighs 7.86 g without the battery, and the complete system with the lithium-ion battery weighs 16.13 g (Figure S30). When worn on the wrist or shoulder, the device conforms to the contour and operates normally under arbitrary deformation (Figures 4E and 4F). The system could undergo a total of 600 cycles of sweat measurement under environmental conditions without obvious deterioration of sensing performance (Figure S32).

AI-assisted sweat fingerprint identification

To understand the sweat fingerprint information captured by the flexible sensing system, we adopted an AI algorithm to analyze the multivariate signals. As illustrated in Figure 5A, six distinct

Please cite this article in press as: Yang et al., An inkjet-printable organic electrochemical transistor array with differentiated ion dynamics for sweat fingerprint identification, Device (2024), https://doi.org/10.1016/j.device.2024.100651

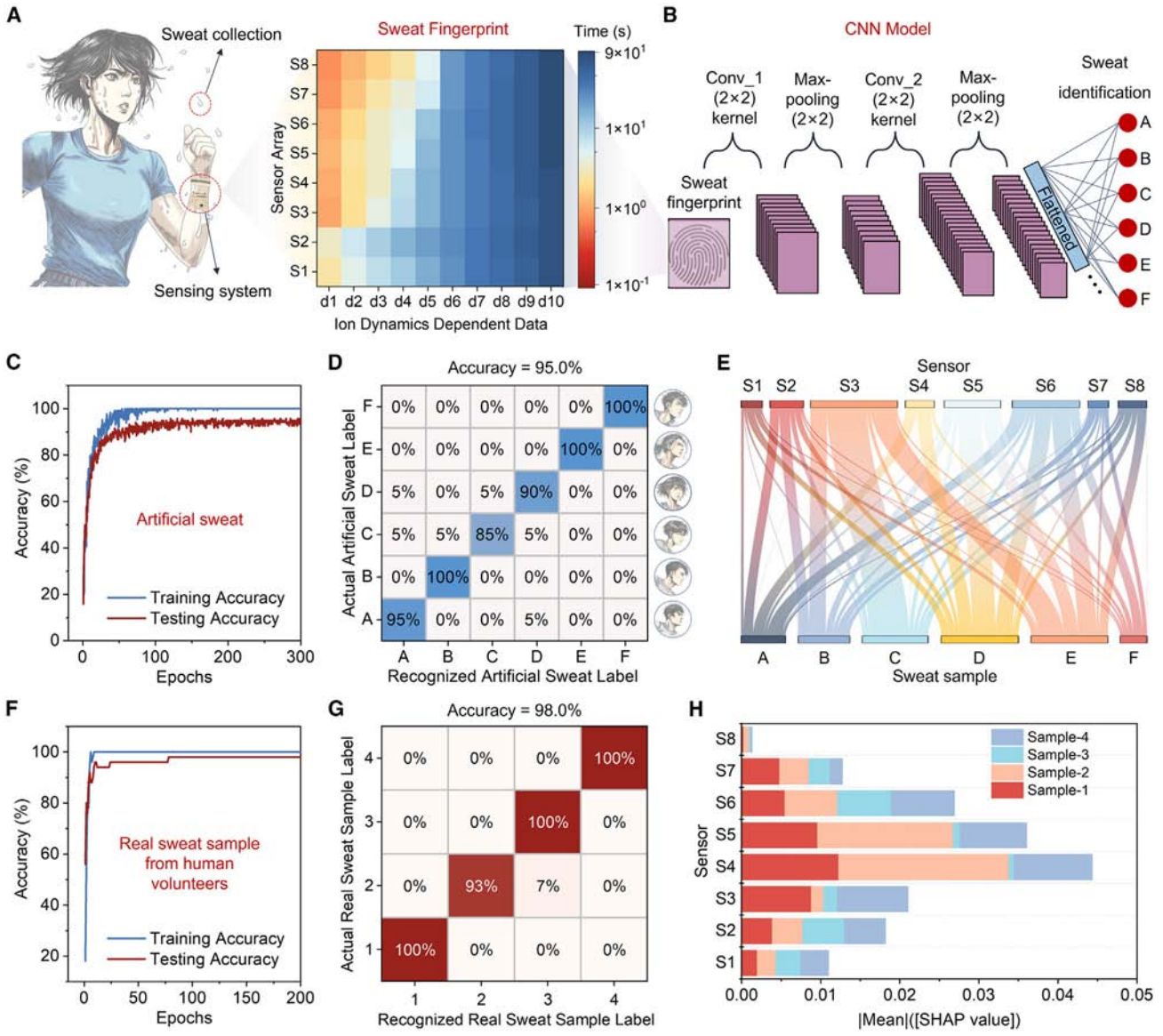

Figure 5. AI-assisted sweat identification

(A) Schematic of sweat fingerprint extraction by the flexible sensing system. The typical sweat fingerprint pattern of artificial sweat C is illustrated. Each pixel represents time data related to ion dynamics in a sensor.

(B) Schematic of the CNN model for sweat identification.

(C) Identification accuracy of artificial sweat during 300-epoch iterations for the training and testing data.

(D) Confusion matrix for test data of 6 samples of artificial sweat. The overall identification accuracy is 95.0%.

(E) Sankey diagram of SHAP analysis depicting the relative contribution of different sensors to sweat classification.

(F) Identification accuracy of real sweat samples during 200-epoch iterations for the training and testing data.

(G) Confusion matrix for testing data of 4 samples of real sweat collected from 4 volunteers. The overall identification accuracy is 98.0%.

(H) Stacked bar plot of sensor importance evaluated by SHAP analysis, showing their contribution to each real sweat sample.

samples of artificial sweat with varying ionic compositions to simulate physiological differences (labeled A–F) were first loaded into the flexible sensing system, and the corresponding sensing current-time (I-T) curves from eight sensors in the differentiated OECT array were collected (Figure S34). Each sample of artificial sweat was measured repeatedly 100 times, forming a dataset of 600 measurements. To collect the ion dynamics-based signals and reduce the computational burden, 10 discrete time-dependent data points were extracted from the sensing I-T curves of each sensor (Note S5; Figure S35), and a total of 80 discrete data points were obtained for each measurement, which were then arranged into an 8 × 10 sweat fingerprint pattern representing the sweat (Figures 5A and S36–S42; Table S4) for training the AI model.

Please cite this article in press as: Yang et al., An inkjet-printable organic electrochemical transistor array with differentiated ion dynamics for sweat fingerprint identification, Device (2024), https://doi.org/10.1016/j.device.2024.100651

We chose to use a CNN algorithm with two convolutional layers, two max-pooling layers, and one fully connected layer (Figures 5B; Note S6) for analyzing the 2D temporal data.[41] The training and testing data were selected randomly at a ratio of 8:2 from the artificial sweat fingerprint dataset. After 300 epochs of training, the identification accuracy for the training and testing data gradually converged (Figure 5C). The confusion matrix of the testing set is illustrated in Figure 5D, verifying the model's performance in classifying six samples of artificial sweat with an average accuracy of 95.0%. To verify the importance of the multidimensional ion dynamics-based features provided by the OECT sensor array, we also trained models using data from each individual OECT sensor within the array (Figure S43). The data obtained from individual sensors were relatively singular and limited, making them more susceptible to external interference and resulting in generally poor predictive capability (~65%–78% accuracy after training). This highlights the role of the OECT array's multidimensional ion dynamics-based information in enhancing robustness and improving identification accuracy. To assess the impact of each individual sensor's features on the final prediction results, we employed Shapley additive explanation (SHAP) for model evaluation. SHAP analysis is designed as a game theory approach in determining a sensor's individual contribution to the prediction and shows the relative significance in the model.[42] As demonstrated in Figure 5E, the SHAP analysis revealed that each sensor in the array contributed to the model's prediction capabilities for each class, indicating that each sensor contained non-overlapping information beneficial to the model, thereby enabling the array-based model to achieve enhanced anti-interference capability and robustness.

To demonstrate the system's identification ability with real sweat samples, we collected sweat from four volunteers of different genders and ages under fixed collection conditions. Each sample of real sweat was measured 25 times, resulting in a dataset of 100 measurements that was split randomly into training and testing sets at a 1:1 ratio. As shown in Figure 5F, the model gradually converged within 200 epochs. The confusion matrix in Figure 5G confirms the model's effective recognition of real sweat samples, achieving an overall recognition rate of 98.0%. The relevance of each feature was evaluated using SHAP analysis as well (Figure 5H). It was established that S4, S5, and S6 were the most influential sensors in predicting real sweat samples, with each sensor in the array contributing to the overall performance of the final model. These results demonstrate that the AI-assisted sweat identification system can efficiently sense and distinguish the information from both artificial sweat and real sweat samples, effectively decoupling intrinsic patterns from complex sweat components.

Next, we demonstrated the potential application of this AI-assisted sweat identification system in disease diagnosis (Note S7). Cystic fibrosis, a genetic disease that can cause extensive damage to the lungs, digestive system, and other organs, is currently diagnosed through a clinical gold-standard test by detecting the chloride ion concentration in sweat.[43] To test our sensor's ability to decouple this particular ion information, Cl^- levels were set at 80 mM for artificial sweat samples A, B, and C, mimicking sweat from patients with cystic fibrosis, and 40 mM for samples D, E, and F as control. Based on the artificial sweat fingerprint dataset, a binary classification task was conducted to distinguish the cystic fibrosis disease with an accuracy of 98.3% (Figure S44).

DISCUSSION

We presented an AI-powered sweat-sensing device for the identification of sweat fingerprints using an inkjet-printable ion dynamics-differentiated OECT array. By using the differential ion screening capabilities of OECT channels with distinct microstructures, we tailored the printing process to customize the channel layer. We developed a porous 3D-IP film and TP film exhibiting ion intercalation-dominated behavior and electron transfer-dominated behavior, respectively. Based on these distinct structures, we designed an OECT array capable of discerning differential ion dynamics, obtaining specific sensing fingerprints for various sweats. As a complete system, the OECT array is integrated with a flexible integrated circuit, a mobile app, and a microfluidic channel, facilitating real-time, multichannel detection of sweat. Integration with a CNN algorithm enabled the identification of sweat samples, underscoring the potential of this system for sweat signal decoupling and human health monitoring.

This sweat fingerprint sensing technology offers a non-invasive solution for health monitoring, disease identification, and, potentially, personal identification. The properties of the OECTs, rather than external modifications, contribute to their enhanced stability. The differentiated ion dynamics design provides information for sweat identification, endowing this approach with anti-interference capability. Further studies across broader users are needed to validate its utility, and the training of a more universal model should account for fluctuations in sweat composition. Extensive datasets will be necessary to enhance the model's robustness and adaptability for real-time sweat analysis. The scalability and low-cost potential of inkjet printing support the technology's market appeal. With optimized ink formulation and printing conditions, the printed devices may be further miniaturized to tens of micrometers, with the overall system footprint reduced to just a few square centimeters. This would reduce the required sweat sample volume, facilitating the development of a larger sweat fingerprint database for enhanced model accuracy. The device currently relies on a flexible yet external AI-powered analysis process. Integrating a compact AI model directly onto the device's hardware could enhance its real-time processing and portability, further advancing the device toward market readiness.

METHODS

Materials and reagents

PEDOT:PSS solution (1.1 wt % in H_2O), PVB, PBS, multiwalled carbon nanotubes (MWCNTs), F-127, Triton X-100, DMSO, and EG were purchased from Sigma-Aldrich. Transparent silver ink (CP 12) was purchased from Mifang Electronic Technology (China). PDMS, NaCl, and KCl were purchased from Sinopharm.

Please cite this article in press as: Yang et al., An inkjet-printable organic electrochemical transistor array with differentiated ion dynamics for sweat fingerprint identification, Device (2024), https://doi.org/10.1016/j.device.2024.100651

Inkjet-printing porous films

The composition of the PEDOT:PSS cocktail ink includes a commercial PEDOT:PSS solution, 6 vol % EG, and 3 vol % Triton X-100. After repeated vigorous stirring for 1 h and ultrasonication for 2 h, the ink was left to stand for half an hour, filtered with a 0.22 μm filter needle, and injected into the inkjet bag. The inkjet printing process was carried out using a microelectronic printer (MP1200, Mifang Electronic Technology) with a 16-channel printing nozzle, which can achieve continuous ink jet of 10 pL ink droplets. To ensure printing accuracy, only a single nozzle is used for printing. Individual droplets are observed through the printer stroboscopic camera (Figure S2). The substrate was cleaned ultrasonically with deionized water, ethanol, and EG; dried with nitrogen; and treated with oxygen plasma for 100 s. Optimal printing droplet spacing (25 μm) and substrate temperature (60°C) were utilized to ensure high precision and film formation, which is discussed in Note S1. The PEDOT:PSS film formed after printing was thermally annealed at 120°C to obtain a 3D-IP film. To obtain the TP film, the 3D-IP film was post treated by repeatedly dropping DMSO onto the film at 120°C for 30 min.

Film characterization

Two-dimensional GIWAXS measurements were conducted on a XEUSS WAXS system (Xenocs, France) with an X-ray wavelength of 1.5418 Å and an incidence angle of 0.2°. Pilatus 300 K (Switzerland) was used as a 2D detector. An atomic force microscope (Bruker, Germany) in a tapping mode with a silicon probe (the elastic coefficient of the cantilever was 40 N/m) was used to characterize the film morphology. The molecular valence bond information was investigated by UV-vis absorption spectra (Shimadzu, UV2600 spectrophotometer, Japan) and Raman scattering spectra with a 532 nm laser (Horiba, HR Evolution, France). X-ray photoelectron spectra were acquired on an AXIS Supra X-ray photoelectron spectrometer (Kratos Analytical, UK) using 150 W monochromatized Al Kα radiation. The appearance of the film formed by the inkjet printing was observed and recorded using optical microscopy (Olympus BX53M, Japan). The HR-TEM images of the films were carried out by a JEM-2100F microscope (JEOL, Japan).

Electrochemical tests

Electrochemical tests were performed using the traditional three-electrode method. Inkjet printing of PEDOT:PSS on fixed-sized Au electrode was used as the working electrode, Ag/AgCl was used as the reference electrode, platinum (Pt) wire was used as the counter electrode, and 1× PBS was used as the electrolyte. The electrochemical tests were performed on an electrochemical workstation (CHI 660E). Specifically, electrochemical impedance spectroscopy was employed with an amplitude of 5 mV, and the range of frequency was 0.01–100,000 Hz.

OECT construction

As illustrated in Figure S11. OECT was constructed using a fully printing method. The electrodes were printed using transparent silver ink. There were two layers of Ag as electrodes. Each layer needed to be annealed at 120°C for 30 min after printing. The width to length ratio (W/L) of the channel is 4, where the length is 0.5 mm and the width is 2 mm. The PEDOT:PSS film was then printed on the reserved channel positions. The gate Ag electrode was then chlorinated (dropping 0.1 M $FeCl_3$ solution for 30 s), and 6 μL of PVB mixed solution (containing 79.1 mg of PVB, 50 mg of NaCl, 1 mg of F-127, and 0.2 mg of MWCNTs dissolved in 1 mL of methanol) was drop coated on the surface to shield the gate electrode from undue oxidation while maintaining a stable potential. Furthermore, a 3D-printed PDMS insulation layer was covered to confine the electrolyte contact to the PEDOT:PSS channel region and ensure no direct contact between Ag and the electrolyte solution. The PDMS base and curing agent were mixed at a weight ratio of 10:1, and the mixture was extruded using a 60-μm-diameter needle to ensure sufficient precision. A fixed-size PDMS water reservoir to store the electrolyte was also 3D printed. Approximately 20 μL of PBS was dropped into the PDMS reservoir to connect the gate and channel.

Electrical and OECT characterization

The current-voltage (I-V) curves, transfer characteristic curves, and output characteristic curves of individual OECTs were measured by a micromanipulator probe station integrated with a semiconductor analyzer (Keithley 4200 SCS). Each device underwent three pre-testing cycles to reach a stable state before actual testing. For better clarity, all I_{DS} values were taken as absolute values. The conductivity (σ) of the film was defined as Equation 1, where W is the width of the channel, L is the length of the channel, and d is the thickness of the film. The d was determined by AFM (Bruker, Dimension Icon, Germany) with tapping mode, and the resistance (R) was calculated by the I-V curves:

$$\sigma = \frac{1}{\rho} = \frac{W}{R \cdot S} = \frac{W}{R \cdot d \cdot L} \quad \text{(Equation 1)}$$

The g_m of the OECT can be as expressed as Equation 2, and the maximum g_m was used to represent the device performance:

$$g_m = \frac{\partial I_{DS}}{\partial V_{GS}} = \begin{cases} \frac{Wd}{L}\mu C^* |V_{GS} - V_T| & (V_{DS} > V_{GS} - V_T) \\ \frac{Wd}{L}\mu C^* |V_{DS}| & (V_{DS} < V_{GS} - V_T) \end{cases} \quad \text{(Equation 2)}$$

The V_T was determined by plotting the square root of the I_{DS} as a function of V_{GS}. The linear portion of the slope with the maximum magnitude is extrapolated, and the intersection with the x axis gives the V_T.

To evaluate the ion-sensing capability of a single OECT, we conducted continuous ion-sensing experiments using 10 μL solutions of different ion concentrations (0.01–100 mM). The solutions were rapidly added and removed to ensure continuity of the sensing curves. V_{GS} was set to 0.4 V to ensure long-term stability and good sensitivity, and V_{DS} was set to −0.1 V.

Flexible sensing system construction

The completed system construction includes the fabrication of an ion dynamics differentiation array, microfluidic chamber

Please cite this article in press as: Yang et al., An inkjet-printable organic electrochemical transistor array with differentiated ion dynamics for sweat fingerprint identification, Device (2024), https://doi.org/10.1016/j.device.2024.100651

construction, and connection to peripheral flexible circuits. First, a differentiated OECT sensor array was constructed using different layers of 3D-IP-OECTs and TP-OECTs. The Ag electrodes at the device interface were designed to be thickened for stable electrical connection. Second, an adapter circuit board was designed to connect the device array to the peripheral flexible circuit (Figure S21). The pins of the adapter circuit and the device were connected using conductive silver paste and cured at 150°C. The adapter circuit board and the peripheral circuit were connected via gold fingers, allowing for multiple insertions and replacements of devices. To fabricate the microfluidic chambers, the PDMS base and curing agent were mixed at a weight ratio of 10:1, and then PDMS microfluidic chambers were formed by inverting custom molds. The PDMS was used to seal the chambers at 80°C, with flexible capillary tubes connected at both ends of the chamber for liquid injection and drainage. The peripheral circuit board, customized according to OECT requirements, was powered by a 3.7 V soft pack lithium-ion battery and integrated with components such as a microprocessor, digital-to-analog converter, and analog-to-digital converter (Figure S24). Low-power Bluetooth was used for wireless communication, allowing simultaneous testing of the transfer characteristics, output characteristics, and I-T curves of eight devices in the array, with results displayed on a customized app (Figure S29). During routine sensing tests, I-T curves were used for testing, and when specific liquids were injected into the microfluidic chambers, the APP interface provided real-time feedback on the response of the OECT array, enabling real-time monitoring and analysis.

Sweat samples

Six samples of artificial sweat samples (A–F) were customized by Dongguan Xinheng Technology, with the primary differences being the concentrations of three key ions: Na^+, K^+, and Cl^-. NaCl concentrations were set at 59.5, 64.5, 69.5, 19.5, 24.5, and 29.5 mM for the six samples, while the KCl concentrations were 15, 10, 5, 15, 10, to 5 mM, respectively. In addition, $CaCl_2$ (2.5 mM) and NH_4Cl (0.5 mM) were kept constant across all samples. As the clinical gold standard for diagnosis, a high Cl^- concentration in sweat (>60 mM) indicates that cystic fibrosis is likely to be diagnosed. To simulate different conditions, Cl^- levels were set at 80 mM for samples A, B, and C, mimicking sweat from patients with cystic fibrosis, and 40 mM for samples D, E, and F, representing normal sweat from healthy individuals. Other components, including glucose (50 μM), lactic acid (10 mM), and uric acid (5 mM), were added to all samples to mimic the complex composition of real sweat and introduce potential interfering substances.

A real human sweat sample was collected from 4 volunteers (3 males and 1 female, aged 20–29 years). Volunteers were instructed to avoid overeating, drinking alcohol, and intense exercise for 24 h before sampling. The following morning, after fasting and performing 30 min of aerobic exercise, sweat was collected from the volunteers' backs. After sampling, impurities in the sweat were removed using a 0.45 μm filter, and the samples were stored in a refrigerator at 2°C. This study was approved by the ethics committees of Peking University (approval number IRB00001052-23101).

Sweat sensing test

To achieve stable sweat sensing and discrimination functionality in our system and to minimize external signal interference, we employed a micro syringe pump, a 20-mL syringe, and a rigid circuit board to conduct sensing experiments (Figure S31). To ensure the proper functioning of all components in the system, a minimum of 0.5 mL of sweat is needed for injection into the PDMS microchamber. During the sweat sensing tests, sweat was injected and extracted at a constant rate of 0.05 mL/s. Initially, deionized water was injected as the background fluid, and the system was run for 100 s to stabilize the baseline. Subsequently, 1 mL of the target sweat was introduced, and the system was allowed to respond for 100 s. The liquid was then extracted, and the chamber was flushed with 5 mL of deionized water for 100 s to restore the baseline. This process marked the completion of one round of the sweat sensing experiment, and subsequent rounds followed a similar procedure.

Machine learning algorithm

A MATLAB program developed in house was employed to preprocess the signals and train the CNN model. The CNN model was developed on a local computer with an individual graphics processing unit module (Nvidia RTX 3060). The signal was denoised by the wavelet filter and then segmented into fixed-length sequences. Further, the sensing data are normalized to extract the data points, which are detailed in Note S5. In summary, the sweat fingerprint figures consisting of ion dynamics-related 8 × 10 data arrays were extracted by analyzing the time constants of different response stages.

The sweat fingerprint figures were fed into a CNN model for the sweat classification task. First, the data are imported and divided into training (80%) and testing (20%) sets. Subsequently, the data are normalized and reshaped into a suitable format for CNN input. The network architecture comprises convolutional layers followed by batch normalization and rectified linear unit activation functions along with max-pooling layers for spatial downsampling. The fully connected layer and softmax layer are employed for classification, with the final layer providing probabilities for each class. The training process utilizes the adaptive moment estimation optimization algorithm with specified parameters, and the model is trained over multiple epochs. In our CNN model, the batch size in the learning model was set to 128 for extracting the feature. The iterative learning rate (LR) was calculated as

$$LR = factor^{\lfloor T/drop\_period \rfloor} * LR_{init} \quad \text{(Equation 4)}$$

where T is the time at the corresponding training process, and the LR_{init} is the initial LR (0.001). The factor is the LR drop factor (defined as 0.1 after 250 periods of training). The max epoch is defined as 300. Performance evaluation is conducted on both training and testing sets, with the accuracy calculated and confusion matrices generated for further analysis, which is detailed in Note S6.

SHAP analysis is designed as a game theory approach in determining a sensor's individual non-overlapping contribution to the prediction and shows the relative significance in the model

instead of building the absolute contribution to sweat identification. When evaluating a sensor, we sum the SHAP values of the 10 features it contains as the total SHAP value of a sensor for the classification result.

RESOURCE AVAILABILITY

Lead contact

Requests for resources should be directed to the lead contact, Yuanlong Shao (shaoyuanlong@pku.edu.cn).

Materials availability

This study did not generate new unique reagents.

Data and code availability

All of the data and figures supporting the findings of this study are provided in the main article or supplemental information. The source code for processing sweat data and training the AI models and the detailed code for SHAP analysis of the CNN's interpretability are publicly available on GitHub (https://github.com/Dongzi-Yang/Code-for-AI-based-Sweat-Sensing-System). Additional data concerned with this work are available from the lead contact, Yuanlong Shao (shaoyuanlong@pku.edu.cn), upon reasonable request.

ACKNOWLEDGMENTS

This project was financially supported by National Natural Science Foundation of China T2188101 (to Y.S.), 52173176 (to L.H.), 51821002 (to L.H.), U2341218 (to M.W.), 62204052 (to J.C.), and 62104042 (to M.W.); Gusu's young leading talent (ZXL2021449); the Key industry technology innovation project of Suzhou (SYG202108); State Key Laboratory of Integrated Chips and Systems SKLICS-Z202315 (to M.W.); and National Key Research and Development Program of China 2021YFB3601200 (to M.W.). We thank Tianjiao Hua for her assistance in creating the illustrations featured in this manuscript.

AUTHOR CONTRIBUTIONS

Yuanlong Shao and D.Y. conceived the idea for the project. D.Y., J.W., M.X., and Y.C. carried out the experiments. X.T. and J.L. assisted with electrochemical testing and analysis. L.H., J.L., and C.S. helped with OECT testing and analysis. M.W. and D.Y. carried out the neural network algorithm and sweat recognition. J.Q. and P.C. provided help with data extraction of the code. L.Z., Z.X., Yanyan Shao, Q.X., and J.C. assisted with the characterization and analysis. Z.Z. and T.L. assisted with sensing analysis. D.Y. wrote the manuscript. Yuanlong Shao, L.H., and M.W. revised and improved the manuscript.

DECLARATION OF INTERESTS

The authors declare no competing interests.

SUPPLEMENTAL INFORMATION

Supplemental information can be found online at https://doi.org/10.1016/j.device.2024.100651.

Received: August 15, 2024
Revised: September 4, 2024
Accepted: November 29, 2024
Published: January 7, 2025

REFERENCES

1. Heikenfeld, J. (2016). Non-invasive Analyte Access and Sensing through Eccrine Sweat: Challenges and Outlook circa 2016. Electroanalysis *28*, 1242–1249. https://doi.org/10.1002/elan.201600018.

2. Nomura, K., Hiyama, T.Y., Sakuta, H., Matsuda, T., Lin, C.H., Kobayashi, K., Kobayashi, K., Kuwaki, T., Takahashi, K., Matsui, S., and Noda, M. (2019). [Na^+] Increases in Body Fluids Sensed by Central Na_x Induce Sympathetically Mediated Blood Pressure Elevations via H^+-Dependent Activation of ASIC1a. Neuron *101*, 60–75.e6. https://doi.org/10.1016/j.neuron.2018.11.017.

3. Broza, Y.Y., Zhou, X., Yuan, M., Qu, D., Zheng, Y., Vishinkin, R., Khatib, M., Wu, W., and Haick, H. (2019). Disease Detection with Molecular Biomarkers: From Chemistry of Body Fluids to Nature-Inspired Chemical Sensors. Chem. Rev. *119*, 11761–11817. https://doi.org/10.1021/acs.chemrev.9b00437.

4. Gao, W., Emaminejad, S., Nyein, H.Y.Y., Challa, S., Chen, K., Peck, A., Fahad, H.M., Ota, H., Shiraki, H., Kiriya, D., et al. (2016). Fully integrated wearable sensor arrays for multiplexed in situ perspiration analysis. Nature *529*, 509–514. https://doi.org/10.1038/nature16521.

5. Bariya, M., Nyein, H.Y.Y., and Javey, A. (2018). Wearable sweat sensors. Nat. Electron. *1*, 160–171. https://doi.org/10.1038/s41928-018-0043-y.

6. Sempionatto, J.R., Lasalde-Ramírez, J.A., Mahato, K., Wang, J., and Gao, W. (2022). Wearable chemical sensors for biomarker discovery in the omics era. Nat. Rev. Chem *6*, 899–915. https://doi.org/10.1038/s41570-022-00439-w.

7. Shao, Y., Ying, Y., and Ping, J. (2020). Recent advances in solid-contact ion-selective electrodes: functional materials, transduction mechanisms, and development trends. Chem. Soc. Rev. *49*, 4405–4465. https://doi.org/10.1039/c9cs00587k.

8. Li, Y., Cui, B., Zhang, S., Li, B., Li, J., Liu, S., and Zhao, Q. (2022). Ion-Selective Organic Electrochemical Transistors: Recent Progress and Challenges. Small *18*, 2107413. https://doi.org/10.1002/smll.202107413.

9. Keene, S.T., Fogarty, D., Cooke, R., Casadevall, C.D., Salleo, A., and Parlak, O. (2019). Wearable Organic Electrochemical Transistor Patch for Multiplexed Sensing of Calcium and Ammonium Ions from Human Perspiration. Adv. Healthcare Mater. *8*, e1901321. https://doi.org/10.1002/adhm.201901321.

10. Pierre, A., Doris, S.E., Lujan, R., and Street, R.A. (2019). Monolithic Integration of Ion-Selective Organic Electrochemical Transistors with Thin Film Transistors on Flexible Substrates. Adv. Mater. Technol. *4*, 1800577. https://doi.org/10.1002/admt.201800577.

11. Xu, S., Kim, J., Walter, J.R., Ghaffari, R., and Rogers, J.A. (2022). Translational gaps and opportunities for medical wearables in digital health. Sci. Transl. Med. *14*, eabn6036. https://doi.org/10.1126/scitranslmed.abn6036.

12. Luo, Y., Abidian, M.R., Ahn, J.H., Akinwande, D., Andrews, A.M., Antonietti, M., Bao, Z., Berggren, M., Berkey, C.A., Bettinger, C.J., et al. (2023). Technology Roadmap for Flexible Sensors. ACS Nano *17*, 5211–5295. https://doi.org/10.1021/acsnano.2c12606.

13. Wang, M., Yang, Y., Min, J., Song, Y., Tu, J., Mukasa, D., Ye, C., Xu, C., Heflin, N., McCune, J.S., et al. (2022). A wearable electrochemical biosensor for the monitoring of metabolites and nutrients. Nat. Biomed. Eng. *6*, 1225–1235. https://doi.org/10.1038/s41551-022-00916-z.

14. Song, Y., Min, J., Yu, Y., Wang, H., Yang, Y., Zhang, H., and Gao, W. (2020). Wireless battery-free wearable sweat sensor powered by human motion. Sci. Adv. *6*, eaay9842. https://doi.org/10.1126/sciadv.aay9842.

15. Rivnay, J., Inal, S., Salleo, A., Owens, R.M., Berggren, M., and Malliaras, G.G. (2018). Organic electrochemical transistors. Nat. Rev. Mater. *3*, 17086. https://doi.org/10.1038/natrevmats.2017.86.

16. Song, J., Liu, H., Zhao, Z., Lin, P., and Yan, F. (2024). Flexible Organic Transistors for Biosensing: Devices and Applications. Adv. Mater. *36*, 2300034. https://doi.org/10.1002/adma.202300034.

17. Paulsen, B.D., Tybrandt, K., Stavrinidou, E., and Rivnay, J. (2020). Organic mixed ionic-electronic conductors. Nat. Mater. *19*, 13–26. https://doi.org/10.1038/s41563-019-0435-z.

18. Kukhta, N.A., Marks, A., and Luscombe, C.K. (2022). Molecular Design Strategies toward Improvement of Charge Injection and Ionic Conduction in Organic Mixed Ionic-Electronic Conductors for Organic Electrochemical Transistors. Chem. Rev. *122*, 4325–4355. https://doi.org/10.1021/acs.chemrev.1c00266.

19. Rivnay, J., Inal, S., Collins, B.A., Sessolo, M., Stavrinidou, E., Strakosas, X., Tassone, C., Delongchamp, D.M., and Malliaras, G.G. (2016). Structural control of mixed ionic and electronic transport in conducting polymers. Nat. Commun. *7*, 11287. https://doi.org/10.1038/ncomms11287.

20. Lan, L., Chen, J., Wang, Y., Li, P., Yu, Y., Zhu, G., Li, Z., Lei, T., Yue, W., and McCulloch, I. (2022). Facilely Accessible Porous Conjugated Polymers toward High-Performance and Flexible Organic Electrochemical Transistors. Chem. Mater. *34*, 1666–1676. https://doi.org/10.1021/acs.chemmater.1c03797.

21. Kim, J.H., Halaksa, R., Jo, I.Y., Ahn, H., Gilhooly-Finn, P.A., Lee, I., Park, S., Nielsen, C.B., and Yoon, M.H. (2023). Peculiar transient behaviors of organic electrochemical transistors governed by ion injection directionality. Nat. Commun. *14*, 7577. https://doi.org/10.1038/s41467-023-42840-z.

22. Tu, D., and Fabiano, S. (2020). Mixed ion-electron transport in organic electrochemical transistors. Appl. Phys. Lett. *117*, 080501. https://doi.org/10.1063/5.0012599.

23. Zhao, C., Yang, J., and Ma, W. (2024). Transient Response and Ionic Dynamics in Organic Electrochemical Transistors. Nano-Micro Lett. *16*, 233. https://doi.org/10.1007/s40820-024-01452-y.

24. Gueye, M.N., Carella, A., Faure-Vincent, J., Demadrille, R., and Simonato, J.-P. (2020). Progress in understanding structure and transport properties of PEDOT-based materials: A critical review. Prog. Mater. Sci. *108*, 100616. https://doi.org/10.1016/j.pmatsci.2019.100616.

25. Xu, C., Solomon, S.A., and Gao, W. (2023). Artificial Intelligence-Powered Electronic Skin. Nat. Mach. Intell. *5*, 1344–1355. https://doi.org/10.1038/s42256-023-00760-z.

26. Xu, C., Song, Y., Sempionatto, J.R., Solomon, S.A., Yu, Y., Nyein, H.Y.Y., Tay, R.Y., Li, J., Heng, W., Min, J., et al. (2024). A physicochemical-sensing electronic skin for stress response monitoring. Nat. Electron. *7*, 168–179. https://doi.org/10.1038/s41928-023-01116-6.

27. Zheng, Y., Tang, N., Omar, R., Hu, Z., Duong, T., Wang, J., Wu, W., and Haick, H. (2021). Smart Materials Enabled with Artificial Intelligence for Healthcare Wearables. Adv. Funct. Mater. *31*, 2105482. https://doi.org/10.1002/adfm.202105482.

28. Wu, J., Liu, H., Chen, W., Ma, B., and Ju, H. (2023). Device integration of electrochemical biosensors. Nat. Rev. Bioeng. *1*, 346–360. https://doi.org/10.1038/s44222-023-00032-w.

29. Hu, H., and Larson, R.G. (2006). Marangoni effect reverses coffee-ring depositions. J. Phys. Chem. B *110*, 7090–7094. https://doi.org/10.1021/jp0609232.

30. Hu, G., Yang, L., Yang, Z., Wang, Y., Jin, X., Dai, J., Wu, Q., Liu, S., Zhu, X., Wang, X., et al. (2020). A general ink formulation of 2D crystals for wafer-scale inkjet printing. Sci. Adv. *6*, eaba5029. https://doi.org/10.1126/sciadv.aba5029.

31. Lee, I., Kim, G.W., Yang, M., and Kim, T.S. (2016). Simultaneously Enhancing the Cohesion and Electrical Conductivity of PEDOT:PSS Conductive Polymer Films using DMSO Additives. ACS Appl. Mater. Interfaces *8*, 302–310. https://doi.org/10.1021/acsami.5b08753.

32. Kim, S.M., Kim, C.H., Kim, Y., Kim, N., Lee, W.J., Lee, E.H., Kim, D., Park, S., Lee, K., Rivnay, J., and Yoon, M.H. (2018). Influence of PEDOT:PSS crystallinity and composition on electrochemical transistor performance and long-term stability. Nat. Commun. *9*, 3858. https://doi.org/10.1038/s41467-018-06084-6.

33. Tu, S., Tian, T., Lena Oechsle, A., Yin, S., Jiang, X., Cao, W., Li, N., Scheel, M.A., Reb, L.K., Hou, S., et al. (2022). Improvement of the thermoelectric properties of PEDOT:PSS films via DMSO addition and DMSO/salt post-treatment resolved from a fundamental view. Chem. Eng. J. *429*, 132295. https://doi.org/10.1016/j.cej.2021.132295.

34. Sessolo, M., Rivnay, J., Bandiello, E., Malliaras, G.G., and Bolink, H.J. (2014). Ion-selective organic electrochemical transistors. Adv. Mater. *26*, 4803–4807. https://doi.org/10.1002/adma.201400731.

35. Wustoni, S., Combe, C., Ohayon, D., Akhtar, M.H., McCulloch, I., and Inal, S. (2019). Membrane-Free Detection of Metal Cations with an Organic Electrochemical Transistor. Adv. Funct. Mater. *29*, 1904403. https://doi.org/10.1002/adfm.201904403.

36. Han, S., Yamamoto, S., Polyravas, A.G., and Malliaras, G.G. (2020). Microfabricated Ion-Selective Transistors with Fast and Super-Nernstian Response. Adv. Mater. *32*, e2004790. https://doi.org/10.1002/adma.202004790.

37. Koutsouras, D.A., Lieberth, K., Torricelli, F., Gkoupidenis, P., and Blom, P.W.M. (2021). Selective Ion Detection with Integrated Organic Electrochemical Transistors. Adv. Mater. Technol. *6*, 2100591. https://doi.org/10.1002/admt.202100591.

38. Strand, E.J., Bihar, E., Gleason, S.M., Han, S., Schreiber, S.W., Renny, M.N., Malliaras, G.G., McLeod, R.R., and Whiting, G.L. (2021). Printed Organic Electrochemical Transistors for Detecting Nutrients in Whole Plant Sap. Adv. Electron. Mater. *8*, 2100853. https://doi.org/10.1002/aelm.202100853.

39. Li, T., Cheryl Koh, J.Y., Moudgil, A., Cao, H., Wu, X., Chen, S., Hou, K., Surendran, A., Stephen, M., Tang, C., et al. (2022). Biocompatible Ionic Liquids in High-Performing Organic Electrochemical Transistors for Ion Detection and Electrophysiological Monitoring. ACS Nano *16*, 12049–12060. https://doi.org/10.1021/acsnano.2c02191.

40. Rivnay, J., Leleux, P., Ferro, M., Sessolo, M., Williamson, A., Koutsouras, D.A., Khodagholy, D., Ramuz, M., Strakosas, X., Owens, R.M., et al. (2015). High-performance transistors for bioelectronics through tuning of channel thickness. Sci. Adv. *1*, e1400251. https://doi.org/10.1126/sciadv.1400251.

41. Li, Z., Liu, F., Yang, W., Peng, S., and Zhou, J. (2022). A Survey of Convolutional Neural Networks: Analysis, Applications, and Prospects. IEEE Transact. Neural Networks Learn. Syst. *33*, 6999–7019. https://doi.org/10.1109/TNNLS.2021.3084827.

42. Scott, M., and Lundberg, S.-I.L. (2017). A Unified Approach to Interpreting Model Predictions. Proceedings of the 31st International Conference on Neural Information Processing Systems, 4768–4777. https://doi.org/10.5555/3295222.3295230.

43. Farrell, P.M., White, T.B., Ren, C.L., Hempstead, S.E., Accurso, F., Derichs, N., Howenstine, M., McColley, S.A., Rock, M., Rosenfeld, M., et al. (2017). Diagnosis of Cystic Fibrosis: Consensus Guidelines from the Cystic Fibrosis Foundation. J. Pediatr. *181S*, S4–S15.e1. https://doi.org/10.1016/j.jpeds.2016.09.064.